Additive Manufacturing 82 (2024) 104035

Contents lists available at ScienceDirect

Additive Manufacturing

journal homepage: www.elsevier.com/locate/addma

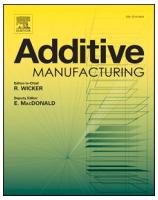

Detection of defects during laser-powder interaction by acoustic emission sensors and signal characteristics

Jun Young Song [a], Adrita Dass [b], Atieh Moridi [b,*], Gregory C. McLaskey [a,*]

[a] School of Civil and Environmental Engineering Department, Cornell University, Ithaca, NY 14850, USA
[b] Sibley School of Mechanical and Aerospace Engineering, Cornell University, Ithaca, NY 14850, USA

ARTICLE INFO

Keywords:
Additive manufacturing
Acoustic emission
Crack
Thermal expansion
And Defect detection

ABSTRACT

Acoustic Emission (AE) sensing is an in-situ real-time nondestructive monitoring method proposed for Additive Manufacturing (AM) to detect defects such as cracks. Previous AE research in AM mainly focused on developing algorithms to automatically detect the defects from AE signals without understanding the physical mechanisms or the signal characteristics that could be used as identifiers. We study AE signals during a laser spot welding on a powder bed to clearly distinguish between different physical mechanisms using their signal characteristics. We identified specific signals associated with 1) tensile cracks from cooling, 2) a powder effect on the substrate, and 3) sudden thermal expansion of the substrate. We used the spectral ratio between high frequency (70–150 kHz) and low frequency (10–40 kHz) spectral amplitudes in the frequency domain to classify and differentiate the source types. We found that porosity due to insufficient energy density did not produce detectable AE signals. Using a ball drop calibration technique, we used AE signals to estimate the absolute sizes of the tensile cracks. Crack sizes ranged from 40 μm to 1 mm and were in general agreement with scanning electron microscope images of the fractures. We performed a line scanning test and successfully validated its potential for the application. Our findings provide a basic understanding of AE signal characteristics in AM, as well as the practical parameters used to separate the signal types.

1. Introduction

Additive manufacturing (AM) is of interest to aerospace, automotive, and biomedical industries [1–9] due to its advantages such as manufacturing complex geometries that cannot easily be made by traditional methods, saving energy and costs, reducing environmental impact, and expediting manufacturing time [10]. However, the quality of AM processing can vary as a function of laser energy, laser scan speed, hatch spacing, powder material, and thickness of the powder bed. If these parameters are not optimized, various types of defects can occur such as 1) keyhole porosity due to instability of the melt pool, 2) lack of fusion defects due to insufficient laser energy density, and 3) solidification cracks [7]. These defects lead to low quality of manufacturing [11,12], so many studies have been focused on the detection and suppression of defects for high mechanical performance of the printed material.

Acoustic Emission (AE) testing has been proposed as in-situ real-time nondestructive method for defect detection [13–15]. As described schematically in Fig. 1, damage sources such as the sudden propagation of a crack can cause a rapid reorganization of the internal stress of the material. This causes the radiation of elastic waves and kHz-frequency vibrations that are detected with sensors and analyzed [13]. Vibrations due to AEs are typically measured with piezoelectric sensors directly coupled or glued to the sample or substrate. Non-contact laser interferometers can also detect AEs [16] and a fraction of the AE vibrations also travel through air and might be detected by a microphone or with the human ear [17] but those are far less sensitive than contact measurements.

Previous studies proposed using AE signal analysis to classify defects such as balling and spatter [17,18], estimate the density of printed material [19], or detect signals associated with keyholing [20,21]. Some studies compared AE results to X-ray computed tomography (XCT) images [21,22] or cross section images [23]. Most of these studies employed machine learning methods to relate continuously recorded AE signals to manufacturing quality and did not focus on the physics of how specific defects could create characteristic AE signals.

In this study, we isolated different mechanisms that produce AEs in an AM environment using simple experiments where defects such as

* Corresponding authors.
E-mail addresses: moridi@cornell.edu (A. Moridi), gcm8@cornell.edu (G.C. McLaskey).

https://doi.org/10.1016/j.addma.2024.104035
Received 8 September 2023; Received in revised form 5 February 2024; Accepted 10 February 2024
Available online 13 February 2024

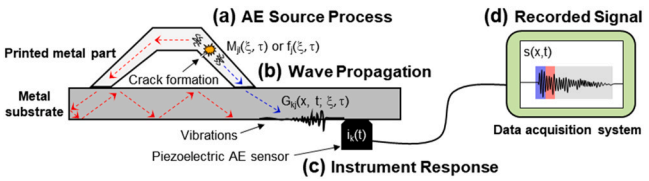

Fig. 1. Schematic diagram of example AE monitoring of a printed part on a metal substrate. (a) The AE source process is exemplified by a tensile crack (orange star), $M_{jl}(\xi, \tau)$, which radiates elastic waves. (b) Wave propagation in the part and substrate is modeled with an elastodynamic Green's function $G_{kj}(x, t; \xi, \tau)$. (c) Piezoelectric sensors convert high frequency vibrations of the surface of the specimen into electrical signals, and this process is represented with an instrument response function $i_k(t)$. (d) Recorded digitized signals are the result of source processes, wave propagation effects, and instrument response (see text).

tensile fracture and pores due to insufficient energy density could be unambiguously separated. Our methods do not replicate current industrial processes; they are a steppingstone toward better understanding the sources and signatures of AEs associated with Laser-powder interaction. Our line scan experiments produced a variety of different signals, described in more detail in Section 5.5, but to further simplify the experiment, we conducted spot welds using SS304 and Ti-6Al-4V powders and used Scanning Electron Microscope (SEM) images of the cross sections to link the different recorded AE signals to visually observed defects. First, a ball drop calibration test was conducted as an absolute reference, and this allowed us to roughly estimate the seismic moment of the AE signals (a measure of the signal's amplitude at low frequencies) which was then used to estimate the physical sizes of the cracks. We also defined time-domain and frequency-domain parameters that were used to discriminate between signals due to tensile fracture from those associated with thermal expansion or powder effect. The spot weld experiments are the primary topic of this paper, but we also discuss how insights gained can be utilized for monitoring of experimental conditions that are more representative of industrial processes.

2. Background on the method of acoustic emission

Acoustic emission signals are recordings of kHz - MHz vibrations generated by rapidly varying forces acting on the surface or interior of a solid (i.e., from sudden crack propagation, ballistic impact, rapid thermal expansion, and other sources). Fig. 1 shows a schematic diagram of an AE signal detected in an AM setting. The AE source, shown as an orange star, is a sudden and localized reorganization of stresses, such as due to the sudden propagation of a microcrack. Elastic waves radiate away from the source location in all directions, reflect off of free surfaces, and cause high frequency surface motions (vibrations) that can be detected by a piezoelectric sensor directly coupled to the metal substrate. The direct arrivals, shown as blue dashed arrows in Fig. 1b and the signals with blue background in Fig. 1d, are the first to be detected by the sensor and contain the most undistorted information about the source. Later arriving reflections, shown as red dashed arrows and red background, also contain information about the source, but are more heavily influenced by the medium through which the waves propagated. Common sources of AE are at most a few μs in duration [24], but the elastic waves generated by AE sources can reflect and refract within the solid thousands of times (i.e. for a few ms) before they naturally decay in amplitude due to intrinsic attenuation in the material (grey background in Fig. 1d). The direct analysis of AE signals can be quite challenging due to the overlap of direct arrivals, Rayleigh waves, and reflected waves; however, the mathematical framework described below and the ball drop calibration source, described in Section 3.3, allows us to quantify the source of the AE signals, despite complications associated with wave propagation.

The processes of AE source generation, wave propagation, and signal recording can be modeled as a set of linear and time invariant systems [25–27]. This framework can be helpful for the inverse problem of characterizing the AE source mechanisms based on recorded signals. We utilize this framework to describe how the AE recording system was absolutely calibrated and how a ball impact source was used to quantify the magnitude of the AE sources and the physical size of the tensile cracks that cause the AE signals.

As shown schematically in Fig. 1, the signal recorded from an AE sensor, s(x, t), can be expressed as the convolution of a source function, a wave propagation function, and an instrument response function. Sources that act on the external surfaces of a body are typically represented by a force vector f_j. In this case,

$$s(x, t) = f_j(\xi, \tau) \otimes G_{kj}(x, t; \xi, \tau) \otimes i_k(t) \quad (1)$$

where $\otimes$ is convolution in time, $G_{kj}(x, t; \xi, \tau)$ is the elastodynamic Green's function that describes how forces in the location ξ at time τ, produce vibrations (displacements) at location x and time t [27,28], and $i_k(t)$ is the instrument response function that describes how a sensor converts a surface displacement vector into a scalar signal and also includes any distortions associated with frequency bandwidth limitations of the sensors, preamp, and digitizer.

Alternatively, sources that occur inside a body such as cracks and earthquakes impart no net linear moment and are typically represented with a moment tensor M_{jl} whose components are force couples acting with opposite sign in the j direction and separated by a distance in the l direction. In this case,

$$s(x, t) = M_{jl}(\xi, \tau) \otimes G_{kj,l}(x, t; \xi, \tau) \otimes i_k(t) \quad (2)$$

where $G_{kj,l}(x, t; \xi, \tau)$ is the first spatial derivative of the Green's function in the l direction.

3. Materials and methods

3.1. Experimental setup for AM

The experimental setup for the custom AM system is shown schematically in Fig. 2, built at the Laboratory of Advanced Materials and Manufacturing at Cornell University detailed in Dass et al. [9,29]. The system is equipped with a 500 W continuous wave laser from IPG Photonics (Model: YLR-MM-AC-500), 500 μm spot size, and 1070 nm wavelength. The laser's working distance to focus on the top of the powder was 207.7 mm. The chamber was made of a steel box (152.4 mm by 152.4 mm by 120.65 mm), which contained a UV-fused silica window at the top to ensure that the laser wavelength passed through the chamber. The chamber was purged with Argon gas to maintain an inert atmosphere during printing.

A Stainless steel (SS304) substrate with dimensions 101.6 mm by

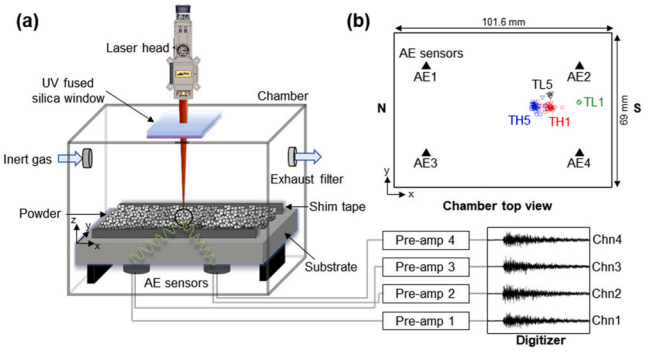

Fig. 2. (a) Schematic diagram of custom AM experimental setup with AE monitoring. (b) Top view of the substrate with dimensions and location of the sensors. The open symbols (e.g., black, blue, red, and green) are AE source locations determined from the array of AE sensors (see Section 4.2).

69 mm by 12.7 mm in the x, y, and z directions, respectively, rested on top of four metallic supports (Fig. 2). Four piezoelectric AE sensors (Panametrics V103, 12.7 mm diameter) were attached to the bottom of the substrate using standard hot glue (Stanley Dualmelt, melting temperature ~135 °C). Sensors were still firmly attached to the substrate after the experiment. This indicated that the hot glue maintained its integrity. Some early experiments were conducted using vacuum grease as a couplant with similar results. Sensors were connected to preamplifiers (Panametrics) with 40 dB gain and 10 kHz to 1 MHz bandwidth. The signals from the sensors were continuously recorded at 10 kHz (low-rate signal) and were simultaneously recorded in a triggered mode where 6 ms-long blocks of data were recorded at 10 MHz (high-rate, triggered signal) when the amplitude of the signal exceeded a specific threshold (above the noise level).

SEM images were obtained for an internal examination of the welded spots after the tests. The cross section of the printed spot was prepared following standard metallographic procedures: grinding and polishing up to 0.05 μm colloidal silica to remove surface imperfections. Then, the polished Back-Scattered Electron (BSE) image was taken using the Tescan Mira3 SEM machine.

3.2. Experimental conditions

We aimed to characterize the source of AE signals by using spot weld experiments and a wide range of processing parameters described in Table 1. In addition to tests with no powder (N), two different powders were used: Ti-6Al-4V (T) and SS304 (S) (Carpenter Additive, diameter: 15–45 μm). For the experiments, we use a multimode laser with a top-hat beam profile with laser power of 300 W (L) and 500 W (H) and dwell time of 1, 3, and 5 seconds. The parameters used here are not representative of current industrial processes. They are designed to repeatedly generate defects in a simplified environment where these processes can be unambiguously separated. There was not a specific reason for the choice of the spot weld locations except that they should be distinct from one another and carefully documented. The same stainless steel substrate was used for all experiments so that only a single calibration experiment was needed, as described below.

3.3. Ball Impact calibration source

We performed a ball drop test prior to the experiments in order to introduce an AE source of known amplitude and frequency content. We dropped a 1 mm diameter steel ball 50 mm onto the substrate without a powder layer. The force-time function of the ball impact can be accurately described using Hertz theory [30].

$$f(t) = F_{max}\cdot\sin(\pi t / t_c)^{3/2} \text{ for } 0 \le t \le t_c \quad (3)$$

$$f(t) = 0 \text{ otherwise}$$

Table 1
Experimental process parameters. Note that the powder layer thickness is 0.5 mm for all powder tests.

Test	Powder	Laser power [W]	Laser duration [s]
NH5	None	500	5
NL5		300	5
TH5	Ti-6Al-4V	500	5
TH3		500	3
TH1		500	1
TL5		300	5
TL3		300	3
TL1		300	1
SH5	SS304	500	5
SH3		500	3
SH1		500	1
SL5		300	5
SL3		300	3
SL1		300	1

In this expression, $F_{max} = 1.917\rho_1^{3/5}(\delta_1+\delta_2)^{-2/5}R_1^2v_0^{6/5}$, the contact duration, $t_c = 4.53(4\ \rho_1^3\pi(\delta_1+\delta_2)/3)^{2/5}R_1v_0^{-1/5}$, $\delta_i = (1-\mu_i^2)/(\pi E_i)$, E is Young's modulus, μ is Poisson's ratio, R_1 is radius of the ball, v_0 is initial velocity of the ball when it impacts, ρ_1 is the density of the ball, and subscripts 1 and 2 refer the material of the ball and the substrate, respectively. The force acts normal to the surface of the substrate (z direction, Fig. 2). The AE sensors used in this work are sensitive to motions in the vertical direction and their instrument response has been previously determined using a ball drop calibration source [31].

In this work, we used the ball impact as an in-situ calibration source to verify all aspects of the monitoring system including sensor coupling and wave propagation in the substrate and to quantify the magnitude of the AE sources recorded during AM process. The magnitude of a seismic source is related to either the change in momentum for external sources or the seismic moment for internal sources and is estimated from the amplitude of the source at low frequencies. For the ball impact this is the change in momentum of the ball, $\Delta P = \int f(t)dt$, or, equivalently, $\Delta P = \Omega_{ball}$, which is the amplitude of the Fourier transform of f(t) at frequencies well below $f_0 = 1/t_c$ (Eq. 3). ΔP can also be calculated from the ball's mass, m, and change in velocity Δv. The initial velocity can be estimated using drop height (h), $v_0 = \sqrt{2gh}$, and the rebound velocity can be measured using the time difference, Δt between the first and second impacts of the bouncing ball: $v_{rebound} = g\cdot\Delta t/2$.

The magnitude of an internal seismic source such as a crack or earthquake is related to the seismic moment, M_0 [32], which is equal to the amplitude of the Fourier transform of the source $M_{jl}(\xi, \tau)$ at low frequencies. These low-frequency amplitudes of external and internal seismic sources, ΔP and M_0 respectively, can be related to one another through a simple constant $C_{FM} = 2c$, where c is the wave velocity in the material where the source originates and the factor of 2 comes from the free surface effect [33]. Using this relation, we estimate the equivalent seismic moment of the ball drop, $M_{0ball} = C_{FM}\cdot\Delta P$. Solids have both longitudinal and shear waves that travel at different speeds, so we assume c is equal to the average of those two waves speeds. Our assumed $C_{FM} = 9100$ m/s should be adequate for a variety of metals (e.g., Steel, Titanium, Inconel, etc.) since variations in wave velocity do not exceed 25%. Variations in C_{FM} due to high temperatures are unlikely to exceed other sources of uncertainty associated with the method [33]; rather, the absolute magnitudes reported here should be considered order-of-magnitude estimates. The 1 mm steel ball we used has $t_c = 3.5$ μs, therefore, $f_0 = 290$ kHz. We used the average amplitude of the Fourier transform of the ball drop signal in a low frequency band (10 – 40 kHz) to determine Ω_{ball}. The seismic moment of an arbitrary AE source, M_{0sig}, is calculated:

$$M_{0sig} = M_{0ball}\cdot\Omega_{sig}/\Omega_{ball} \quad (4)$$

where Ω_{sig}, is the average amplitude of the Fourier transform of the AE signal in the 10–40 kHz frequency range.

4. Results

4.1. Signal overview

Fig. 3 shows representative examples of AE signals recorded from three different tests: Ti-6Al-4V powder, SS304 powder, and no powder. In each test, the 500 W laser was activated for a duration of 5 s while the stage remained stationary. The signals plotted in the left panels (Figs. 3a, 3c, and 3e) are the low-rate, continuously recorded data from Channel 1 and insets show zoomed in sections of the signals generated when the laser was first turned on. Signals shown in the right panels (Figs. 3b, 3d, and 3f) are from high-rate triggered data, also from Channel 1, with a zoomed-in time scale to highlight the differences.

We repeatedly observed significant differences in the types of signals produced by the tests on different powders. Tests on the Ti-6Al-4V powder produced swarms of impulsive AE events that primarily

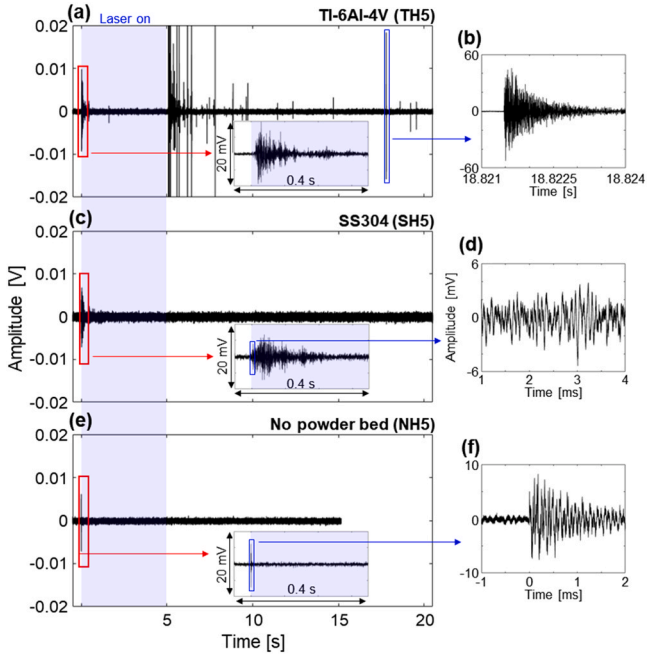

Fig. 3. Overview of signals measured with different powders and 5 s laser duration (blue shaded area): (a and b) Ti-6Al-4 V powder (TH5, see Table 1) and (c and d) SS304 powder (SH5) and (e and f) no powder (NH5). Note the swarm of impulsive AE signals in (a) that occurred just after the laser was turned off (see text). For the experiment shown in (e), the recording system was stopped after 15 seconds.

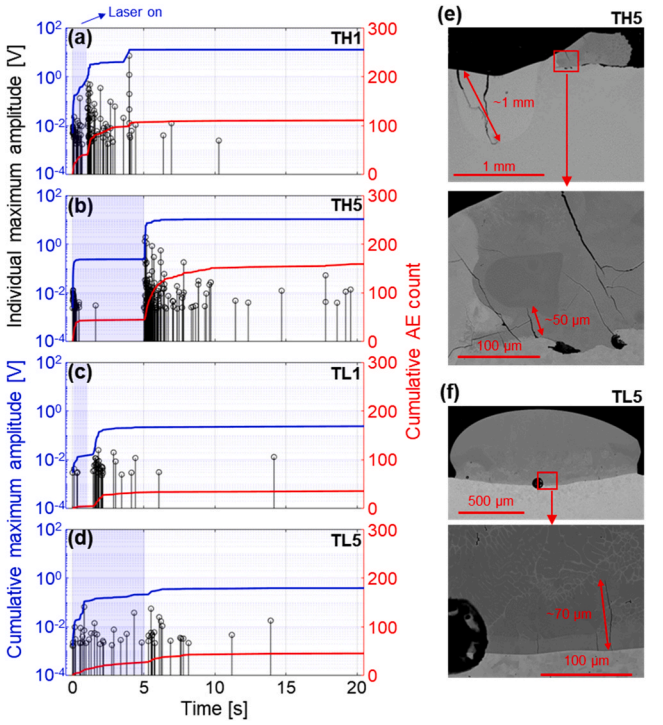

Fig. 4. Maximum amplitude of each triggered signal (black), cumulative maximum amplitude (blue), and cumulative AE count (red) in Ti-6Al-4V powder tests (a) TH1, (b) TH5, (c) TL1, and (d) TL5. SEM images of welded cross section in (e) TH5 and (f) TL5.

occurred when the laser was turned off and continued sporadically for tens of seconds. In contrast, tests on the SS304 powder and tests with no powder only produced AE signals when the laser was first turned on (Figs. 3c and 3e). When no powder was present, this initial signal was abrupt and short-duration. It decayed back to the noise level after only ~3 ms (Figs. 3e and 3f). When powder was present, the initial signal was not abrupt, was lower amplitude, had an extended duration (~200 ms), and consisted primarily of lower frequencies (Fig. 3a inset, 3c inset, and 3d).

4.2. AEs and fractures in Ti-6Al-4V

Fig. 4 shows the AE and SEM results of Ti-6Al-4V powder tests. The maximum amplitude of each triggered AE signal (black circles with stalks) is shown alongside the cumulative maximum amplitude of the AE signals (blue) and cumulative counts of AE events (red) over time (Figs. 4a to 4d). SEM cross section images were taken at the spot where the laser hit the substrate (Figs. 4e and 4f). Recorded AEs were almost exclusively impulsive events that were rich in high frequency energy up to 1 MHz. We term these "crack" signals, since their features are similar to AEs observed to be associated with microcracks in rock and concrete [34].

The maximum amplitude of the AE signals is larger in test TH5 (Fig. 4b) than in TL5 (Fig. 4d) and corresponding SEM images show larger cracks (~1 mm) in TH5 (Fig. 4e) than in TL5 (Fig. 4f), which are 20–70 µm. In Section 5.1.2, we outline how the physical size of the crack can be determined from the amplitude of the AE signal. We were able to use the timing of the abrupt first wave arrivals measured from signals recorded from the array of sensors to triangulate the source locations of the AEs, following standard techniques [35]. Though there was some scatter in the results (+/- 1.4 mm standard deviation), we were able to confirm that signals originated from the designated weld spot, and we could clearly identify the separate locations of tests (see Fig. S1 for the method and Fig. 2b for the result). The timing of the AEs generated during these tests indicates that the majority of the AEs and the largest AEs occurred soon after the laser was turned off, while AEs continued to occur sporadically for tens of seconds in a decaying manner. Some smaller AEs occurred immediately after the laser was turned on, but AEs were mostly absent while the laser remained on.

The melting mode can be delineated through the aspect ratio of the melt pool, which is defined by the ratio between the penetrated depth and width. The boundary of keyhole mode and conduction mode is characterized by the aspect ratio ranging from 0.4 to 0.8 [36–38]. The SEM image clearly demonstrates that TH5 exhibits the aspect ratio of ~1, indicative of the keyhole mode. In contrast, TL5 barely penetrates the substrate, so it is closer to the conduction mode. The solidified melt was scattered with a solidified wing of Ti-6Al-4V powder in TH5 and many cracks in the melted part ranging from 50 µm to ~1 mm in length (Fig. 4e). However, the solidified part in TL5 shows a more circular shape with small size of cracks, ~70 µm in length. As seen in AE counts (Figs. 4b and 4d), the number of detected cracks in TH5 were ~3 times higher than that in TL5 and the amplitude of the largest AE signals in TH5 was also 10x higher than TL5. Similarly, the SEM images show more cracks and larger cracks in TH5 (Fig. 4e) than in TL5 (Fig. 4f).

4.3. Porosity and powder effect signal in SS304

Fig. 5 shows SEM images and AE signal characteristics from tests with SS304 powder. Different from the Ti-6Al-4V samples, all the SEM cross-section images showed circular solidified melt (~1 mm diameter) with different amounts of porosity. From the processing conditions listed in Table 1, the absorptivity of ~0.3, and the estimated 1–2 mm^3 volume, calculated volumetric energy densities indicate that SH1, SL3, and SL1 should exhibit porosity due to insufficient energy density, whereas SH5, SH3, and SL5 were closer to conduction modes. Pores were formed in most SS304 conditions presented here due to insufficient input of laser energy density, resulting in incomplete melting of the powder particles within the affected volume and causing irregular pore morphologies [39]. Consistent with expectations for defects due to insufficient energy

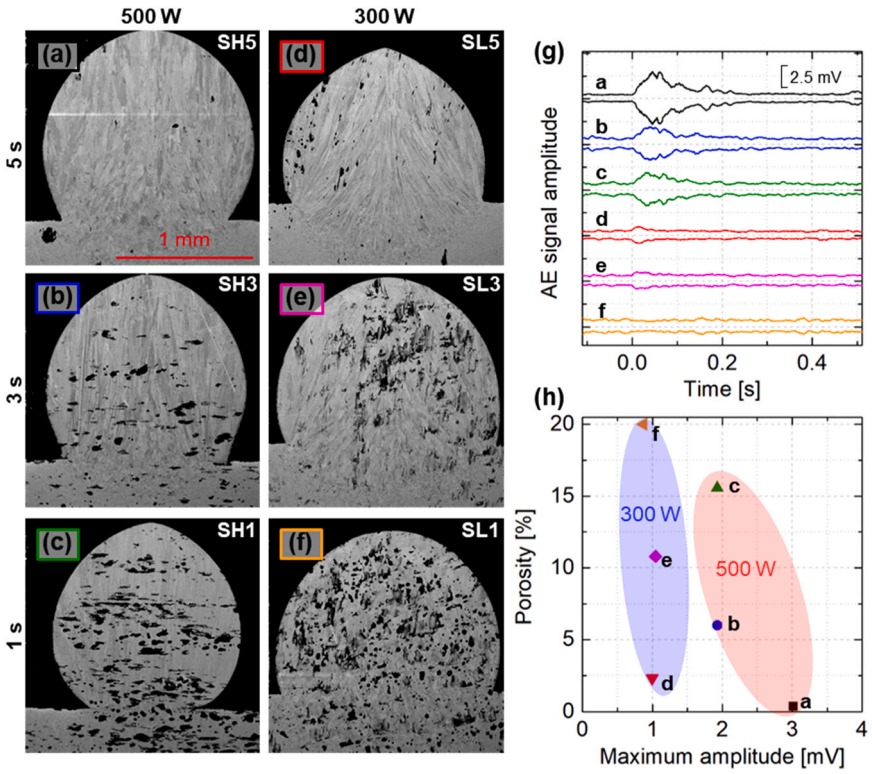

Fig. 5. SEM images of cross sections of experiments with the SS304 powder with different laser energy and duration: (a) SH5, (b) SH3, (c) SH1, (d) SL5, (e) SL3, and (f) SL1 (See Table 1 for a list of tests). (g) The envelope of the signals, calculated from low-rate signals in Channel 1, see text. (h) The relationship between porosity calculated from SEM images and maximum amplitude from the envelope of the signals in (g).

density, we observe a reduction in porosity with increasing dwell time (SH5 and SL5) and increasing laser power. As mentioned previously, detectable AE signals were only produced when the laser was first turned on (Fig. 3c). These signals were not typical AEs and were in many ways different from the "crack signals" described in the previous section. They have small amplitude, had an extended duration, were depleted of high frequency energy, and were not impulsive, so they could not be located. We do not consider them AE events; they are more similar to a transient noise and would not be detected by many AE monitoring systems. We term this category of signal "powder effect" signals since they were observed for tests with a powder layer (both Ti-6Al-4V and SS304), but not for tests without powder.

Fig. 5g shows the +/- envelope of the amplitude of the acoustic signal over time. The envelope shown is a 10 ms moving average of the root-mean-square of the signal collected from the low-rate signals from Channel 1. The first signal in Fig. 5g (black color) is derived from the same signal as Fig. 3c. The AE signal amplitude was larger with higher laser energy. Note that our 10 ms moving average effectively limits the bandwidth to 100 Hz, which allows us to use the continuous low-rate recorded signal sampled at 10 kHz. All other analyses in this study used high-rate signals sampled at 10 MHz.

To test if the AE signals were related to the observed porosity, Fig. 5h shows the maximum amplitude of the AE signal envelope against the porosity, showing essentially no correlation. Porosity, defined as the ratio of the pore area and the area of the circular region, was quantified in the binarized image using the thresholding method. At the same laser duration, the maximum amplitude was smaller with 300 W laser energy than that with 500 W, but porosity was higher. This implies that the AE signal amplitude may be affected by the laser energy, but it does not have a direct correlation with porosity.

4.4. Signal characteristics

In this section, we describe the different AE signals in both the time and frequency domain. Fig. 6a shows representative examples of three different types of signals on an identical time scale: 1) crack signals, produced from the Ti-6Al-4V tests, 2) powder effect signals from SS304 and Ti-6Al-4V, and 3) the signals produced when the laser was first turned on during in tests with no powder, which we term "thermal expansion". The example signals from the cracks are from the data shown in Fig. 4b and occurred after the laser was deactivated at ~5.1 s for the large crack and ~5.8 s for the small crack. The example powder effect signals are from Fig. 3c. The thermal expansion signal is the first arrival of the signal shown in Fig. 3f. Similar to the crack signals, the thermal expansion exhibits an abrupt increase in amplitude upon the first arrival.

Fig. 6b shows the Fourier transform of the signals in Fig. 6a using a 2 ms time window. The different signals differ in both absolute amplitude and relative spectral shape. The crack signals contained the most high frequency energy while the thermal expansion and powder effect signals have spectra that are more depleted in the 100 kHz frequency band. We focused on two frequency bands denoted low (10–40 kHz) and high (70–150 kHz). We chose these frequency bands because of their good signal-to-noise ratio and because the low frequency band was below the corner frequency f_0 of the ball drop calibration source; however, different frequency bands that are sufficiently separated (i.e. 50–75 kHz and 300–450 kHz) could also be used for signal discrimination, depending on sensor properties or bandwidth limitations of the recording system. The average amplitude in the low frequency band was taken to be a measure of the size of the source or the seismic moment. We define the spectral ratio as a second discriminating parameter. It is the ratio of the average amplitude in the high frequencies band (A_{high}) to the average amplitude in the low frequency band (A_{low}), expressed in decibels (dB) such that spectral ratio $= 20 \cdot \log_{10}(A_{high} / A_{low})$. The crack

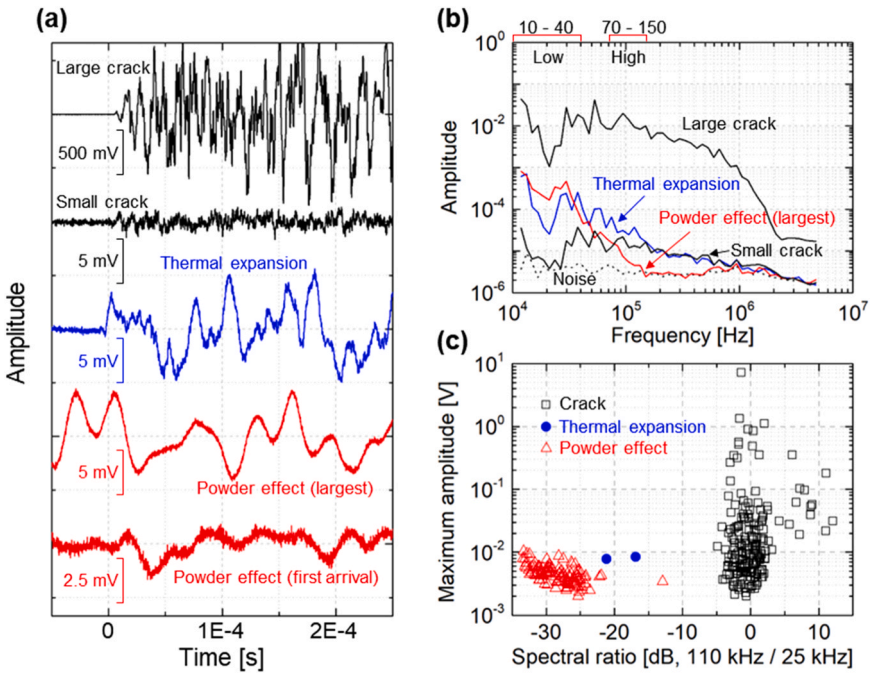

Fig. 6. (a) Representative high-rate signals of large crack (TH5, see Table 1), small crack (TH5), thermal expansion (NH5), and powder effect showing both the first arrival and largest amplitude signals (SH5) and (b) the amplitude of the Fourier transform of the signals in (a). Note that the time window used to compute the Fourier transform was 2 ms. (c) Spectral ratio against the maximum amplitude in the time domain of all tests (see text).

signals varied greatly in amplitude, but all exhibited a spectral ratio near 1. The thermal expansion had a distinctly smaller spectral ratio of 0.1 (−20 dB) while the powder effect signal had a spectral ratio that was even lower.

Fig. 6c maps the data blocks containing various AE signals using the maximum amplitude and spectral ratio. However, we used the signal maximum amplitude in the time domain instead of the seismic moment of the events (a frequency domain parameter), since those two quantities are generally proportional, as shown in Fig. 7. For the cracks and thermal expansion, we confirmed that the signal-to-noise ratio (SNR) was greater than 10 dB in both the low frequency band and high frequency bands. For the powder effect signals, SNR was > 10 dB in the low frequency band, but not in the high frequency band. As a result, spectral ratios for powder effect signals shown here should be taken as upper bounds and could be much lower. Powder effect signals had spectral ratios of −25 dB to −35 dB meaning that the amplitude at low frequency band is at least 18–56 times higher than at high frequency band. An anomalous powder effect data point shown in Fig. 6c has a spectral ratio of −13 dB, much larger than the rest. This signal overlapped with some unknown source of 75–100 kHz energy that may have been due to a very small fracture or mechanical oscillation of some sort. Thermal expansion signals had intermediate spectral ratios that were larger than the powder effect signals, but far below the cracks.

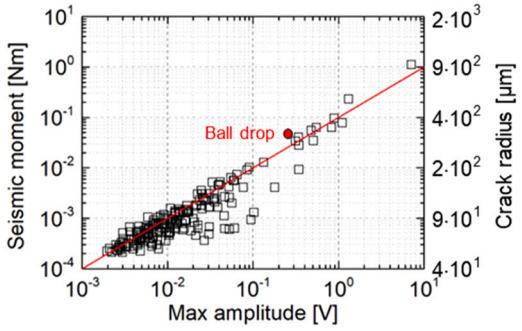

Fig. 7. Maximum amplitude of high-rate signal in time domain and seismic moment calculated from the amplitude in frequency domain at low frequencies. Note that all the signals from Ti-6Al-4V powder tests in Channel 1.

5. Discussion

5.1. Cracks in Ti-6Al-4V

This study is not intended to identify the causes of cracks or to optimize printing parameters to prevent cracks or other defects. Instead, we chose parameters where defects could be consistently created and we focused on the discrimination of the AE signals associated with those defects. For tests on SS304, we did not observe microcracks in the SEM cross sections and we did not observe any impulsive AE events. However, for Ti-6Al-4V tests, we consistently observed many microcracks in all the SEM cross sections and we detected sequences of impulsive AE events, as described in Section 4.2. This behavior happens because unlike SS304, Ti-6Al-4V forms intermetallic compounds with the SS304 substrate. These brittle compounds are prone to cracking due to tensile stresses induced by the cooling [40,41]. We also do not observe impulsive AE events during the tests without powder, except the single event when the laser was first turned on, labeled thermal expansion. We also located the AE sources to verify that they are coming from the location of the spot weld. This eliminates the possibility of spurious AE sources such as from sensor coupling, or the substrate supports. As shown in Fig. 4, the majority of the impulsive AE events occurred when the laser was turned off and continued sporadically for tens of seconds. This time evolution suggests that the AEs are from thermal cracks that occurred due to tensile stresses induced by the cooling process [41]. Note that in experiment TL5 (Figs. 4d and 4f) there are fewer cracks overall, but still a cluster of AEs were observed when the laser was turned off, between 5 and 6 seconds. We also note that AEs continued to occur for 10 s of seconds after the laser was turned off, and this is distinct from the decay of the reverberations that occurs after each individual AE event. It takes ~3 ms for the elastic waves generated from one impulsive AE event to decay back to approximately the noise level, shown schematically as the section of the signal with a gray background in Fig. 1d.

In contrast, impulsive AE events continued to occur, intermittently, at a rate that decayed over 10 s of seconds, presumably as the specimen cooled.

5.1.1. Correlation of parameters in frequency domain and time domain

The correlation between seismic moment and maximum amplitude of triggered signals in Channel 1 is plotted in Fig. 7. The maximum amplitude and seismic moment are linearly correlated (slope of 1 on log-log plot) regardless of laser energy and duration time. The Pearson correlation coefficient, γ_{xy}, can be used to estimate the linear statistical relationship [42,43]. In Fig. 7, the γ_{xy} value calculated for log-scale data is 0.924, indicating a strong linear correlation, as a value of 1 denotes perfect linearity. This linear proportionality exists because the low frequency range (10–40 kHz) used to estimate the seismic moment is also typically the frequency band with the largest amplitude (Fig. 6b). Note that if a different frequency band was chosen or if a different sensor was used with a different frequency response, then seismic moment and maximum amplitude may not be linearly proportional or may have a different proportionality constant.

5.1.2. Estimation of the physical size of cracks from the AE signal

We roughly estimated the physical size of cracks causing an AE signal by assuming that the seismic moment M_0 is approximately equal to the amplitude of the components of the time independent source moment tensor D_{ij}. Following [44], the moment tensor of an opening crack has the form:

$$M_0 \approx D_{33} = (\lambda + 2)\cdot b\cdot dA \tag{5}$$

where 2b is the crack opening, dA is the fracture surface area, $\lambda = \nu\cdot E/(1+\nu)(1-2\nu)$ is the Lamé parameter, $\mu = E/2(1+\nu)$ is the shear modulus, E is the Young's modulus, and ν is the Poisson's ratio. This formulation assumes the area of the microcrack, dA, is in the x_1-x_2 plane and the crack opening direction is x_3, but changing this orientation will cause variations of only a factor of 2. We then assumed a circular elastic fracture of radius a with an elliptical cross section with maximum crack opening at the center [44,45]:

$$2b = [4(1-\nu)/(\pi E)]\cdot\sigma\cdot a \tag{6}$$

where σ is the stress change acting on the fracture surface. Plugging Eq. 6 into Eq. 5 and assuming the crack volume from a half-elliptical shape, we found:

$$dV = b\cdot dA = 2/3\pi\cdot a^2\cdot b \tag{7}$$

$$M_0 \approx K\cdot\sigma\cdot a^3 \tag{8}$$

where $K = 4(1-\nu)\cdot(\lambda+2\mu)/3E = 4(1-\nu)^2/[3(1+\nu)\cdot(1-2\nu)]$. Thus, $K \approx 1.3$ when $\nu \approx 0.3$. We can then solve for the crack radius a from Eq. 8:

$$a \approx [M_0/(K\cdot\sigma)]^{1/3} \tag{9}$$

This is essentially identical to an expression used in the study of earthquakes derived from the expressions $M_0 = \mu AD$ and $\Delta\sigma = C\mu D/a$ (Eq. 1 and 5 from Kanamori and Anderson [46]) by solving the second equation for D and inserting it into the first equation. In the previous expressions, A is the rupture area, D is the average fault slip over the rupture area, C is shape factor, and Δσ is the shear stress drop.

For tensile fracture of metal, σ in Eq. 9 is equal to the yield stress of the material, since the stresses felt on the crack surfaces likely drop from the yield stress to zero (free surfaces). Plugging realistic values for Ti-6Al-4V ($\sigma = 880$ MPa and $\nu = 0.34$ so $K \approx 1.4$) into Eq. 9, we obtained an expression for the crack radius in meters when the unit of M_0 is Nm:

$$a = (M_0/1.232e9)^{1/3} \tag{10}$$

Since the seismic moments varied from 10^{-4} Nm to 1 Nm (Fig. 7), the corresponding crack radii ranged from ~40 μm to ~1 mm. This range is in reasonable agreement with the maximum crack length found from the SEM images (~1 mm in Fig. 4e). Moreover, the triggered signals in TL5 (Fig. 4d) exhibited $\sim10^{-2}$ maximum amplitude, corresponding to ~90 μm crack radius, and this also aligns with the observations from the SEM image (~70 μm in Fig. 4f). We admit that this corroboration between recorded AEs and SEM images is somewhat rough: we cannot know if the cracks in the SEM images opened in a single event or if they formed in multiple episodes and would therefore produce multiple AEs. There are also significant sources of uncertainty associated with the theory outlined above and with the absolute estimation of the M_0 from the recorded AE signals. We therefore consider the calculation of crack radii absolutely accurate only to a factor of 3, but we note that the range of crack sizes estimated for our population of AE signals closely aligns with the sizes observed in SEM images.

5.2. Thermal expansion (Bare substrate)

Rapid thermal expansion of the substrate due to a laser pulse [47,48] has previously been used as a standardized AE source [49]. In our experiments, we observed a signal when the laser was first turned on (Fig. 3e), which we term "thermal expansion" (Section 4.4). We only found this signal in tests with no powder; the presence of the powder likely blocked the substrate from the laser and caused a longer-duration, lower-amplitude signal that we term "powder effect", described below. We can be sure of this result because a thermal expansion signal would have been detected based on its higher frequency content compared to the powder effect signal. While detection of this signal likely has little application in practical AM applications, it highlights how the AE signal parameters identified can be used to effectively discriminate cracks signals from other AE sources (Fig. 6c).

5.3. Powder effect

As seen in Section 5.1, tests with powders did not produce abrupt thermal expansion signals, but did produce "powder effect" signals that were not impulsive, small in amplitude, and lasted ~0.2 s long. We do not fully understand the physical mechanism of this signal, but we know that it occurs when a laser first interacts with a powder layer. We observe such a powder effect signal with both the Ti-6Al-4 V and SS powder beds, despite those prints having extremely different quality. We do not observe the powder effect signal for the tests with no powder bed. The signal is likely due to the partially melted powder falling onto the substrate as the laser first hits it [50]. Such an AE source would be the cumulative effect of many tiny particle impacts or a diffuse thermal expansion effect, and this could account for the extended duration and low frequency dominance of the powder effect signal compared to the other signals. In fact, the extended duration, lack of high frequencies, and lack of abrupt onset observed for the powder effect signal are in many ways similar to tremor signals detected deep in the Earth, which are thought to be composed of myriad weak earthquake events [51]. The line scan results, described in Section 5.5, add further support for our interpretation because numerous powder effect signals were produced while the laser was actively scanning over new powder, and no powder effect signals were detected when the laser was stopped, despite the presence of crack signals and vibrations due to movement of the stage. Fig. 5g shows that the amplitude of the powder effect signal increases with increasing laser power but is not affected by the laser duration or porosity of the print.

5.4. Pores

The SS304 tests exhibited pervasive porosity; however, we found that the amount of porosity was not correlated with the amplitude or characteristics of the AE signals (Fig. 5). Based on this, we conclude that porosity does not produce a detectable AE signal. However, Ito et al. [23] suggested that pores due to keyholes at high energy density were

accompanied by strong AE signals. In that work, pores with 50–100 μm diameter presumably generated signals with ~100 mV maximum amplitude and were some of the largest signals detected in that study. Note that it is difficult to directly compare the amplitudes of AE signals collected using different sensors and experimental setups without taking into account differences in sensor sensitivity, amplification, and wave propagation. Seleznev et al. [21] found many residual pores when the powder was overly melted by the laser which is the same as the keyhole mechanism. However, there were no detectable AE signals in the overly melted zone. Instead, noticeable AEs were found in regions with cracks. Ito et al. [23] also showed many cracks around the pores, so there is a possibility that cracks (perhaps associated with the pores) generated the AEs rather than the pores themselves.

5.5. Extension to line scan and multilayer prints

The spot weld experiments presented so far in this study are not representative of current industrial practices. However, we believe that the signal discrimination techniques and insights made here can be applicable to more complicated cases of line scans and multilayer prints in an environment where additional noise sources are present. To demonstrate, we conducted a line scanning experiment (300 W laser energy, 15 mm/s scanning speed) using Ti-6Al-4V powder, as shown in Fig. 8. The sensor distribution is similar to the spot weld experiments and the signals shown are from Channel 1 (Fig. S2). The maximum amplitude of each triggered AE signal is shown over time (Fig. 8a) with red for powder effect and black for crack, based on the parameters described in Section 4.4, shown in Fig. 8d. Different from the spot weld experiments, we observed far more AEs and we observed numerous powder effect signals while the laser was actively scanning, rather than only when the laser was first turned on (Fig. 3).

Similar to the spot weld experiments, we detected a swarm of crack signals after the laser was turned off, and these persisted sporadically for many seconds. Fig. 8b presents representative signals of the powder effect and cracks. Fig. 8c shows the recorded AE signals and focuses on the first few seconds of the experiment. The blue signal is from another sensor mounted near the laser head, far from the substrate. It shows vibrations due to movement of the stage. The laser was turned on at ~0.5 s before the stage started moving. The stage then moved for ~1 s, paused, and then returned to its original position after the laser was turned off. Fig. 8d shows the AE signals mapped onto the same parameter space shown in Fig. 6c. Once again, this allows for clear differentiation between cracks and other noise sources such as the powder effect signals. We note that with the application of a high-pass filter, crack signals can be detected even amid other simultaneous signal sources such as powder effect signals and mechanical vibrations.

While the application of these methods to multilayer builds and conditions similar to current AM practice is outside the scope of this study, we note that the addition of a complicated part, as shown schematically in Fig. 1, will only add an additional effect to the wave propagation component (G_{kj}) of the recorded signal. Such an addition will likely distort signals on the 1–10 μs time scale and could potentially produce a resonance of the part that would affect the overall shape of the spectra of the AE signals. The former would make source location more difficult and the latter would potentially affect the absolute value of the parameters of Fig. 8d, but would not affect the relative differences that can be used to differentiate cracks from other sources. Overall, the changes outlined above would not have a strong effect on our ability to measure (1) the abruptness of the sources and the spectral ratio parameter, (2) the timing of the sources, (3) the absolute amplitude of the source (since attenuation is low in metallic materials), and (4) the variety of AE sizes observed. We believe that the main insights from this study remain unchanged. Cracks can be easily detected amid other, lower frequency sources associated with powder effects and mechanical noise, physical crack size can be estimated using absolute calibration, and pores do not produce detectable AE signals.

6. Summary and conclusions

We studied the method of AE for monitoring defects during AM process due to its advantages of being a real-time nondestructive technique. Different from previous studies focused on signal classification without a proper understanding of the signal origins, we investigated the individual signal characteristics and underlying physical mechanisms of

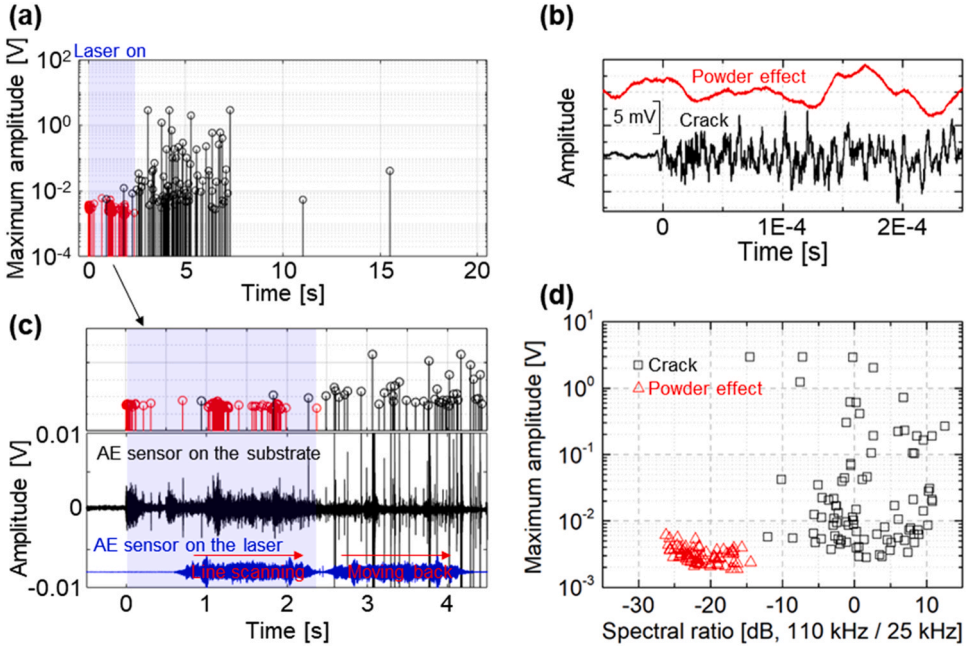

Fig. 8. Line scanning experiment with 300 W laser energy and 15 mm/s scanning speed. (a) Maximum amplitude of triggered signals with time. (b) Powder effect signal (red) and crack signal (black) as representative examples. (c) Overview of the signal when the laser was activated, with the AE sensor on the laser (blue) capturing the laser movement. Note that the first movement (0.8 s to 2.3 s) is line scanning whereas the second movement (2.5 s to 4.2 s) is the stage moving back while the laser is off. (d) Spectral ratio plotted against the maximum amplitude in the time domain.

AEs generated during spot welds in a simplified experimental system that did not replicate current industrial processes but allowed us to link AE signal parameters to their physical mechanisms. Three types of AE signals could be clearly distinguished: 1) powder effect, 2) thermal expansion, and 3) cracks. We also utilized a ball drop test to calibrate the AE recording system and determine the absolute seismic moment of the AE sources, which was then used to estimate the physical size of the cracks that produced the AE signals. The calculated size distribution (40 μm - 1 mm) was generally consistent with the sizes of cracks observed in SEM images and tests with smaller observed cracks also had AEs with smaller maximum amplitude. From the analyzed data, the following observations and conclusions can be drawn:

1. A ball drop test was conducted for the absolute calibration of the AE recording setup and the calculation of seismic moment or size of the AE signals.
2. The physical size of the cracks was estimated from the absolute seismic moment of the recorded AEs. The calculated crack sizes approximately matched with crack sizes found from SEM images.
3. In tests with no powder, an abrupt, short duration (2 ms) signal was detected only at the beginning of the laser heating despite the fact that the laser continuously heated the substrate. This signal was induced by sudden thermal expansion of the substrate. This type of signal did not occur for tests with powder.
4. In tests with a powder, an extended duration (~0.2 s) "power effect" signal was detected when the laser was first turned on. These signals were low amplitude, deficient in high frequency signal energy compared to other types of signals and lacked abrupt first arrivals. These characteristics, and the increased number of powder effect signals observed during line scans, are consistent with the idea that the source of the signal is from hot powder hitting the substrate and producing a diffuse thermal expansion signal.
5. Ti-6Al-4V powder tests produced tens to hundreds of abrupt, short duration AE signals with a range of amplitudes. They mostly occurred during solidification and for many seconds after the laser was turned off. SEM images of samples from these tests showed cracks.
6. Pores do not appear to produce AE signals; porosity was not correlated with the amplitude or characteristics of the signals recorded.
7. The spectral ratio of high-frequency (70–150 kHz) to low-frequency (10–40 kHz) energy in the AE signals was the primary parameter used to discriminate between different AE sources. Cracks had spectral ratios near 0, while the powder effect signals had spectral ratios that were at least 30 dB lower. Thermal expansion signals had an intermediate spectral ratio between that of the cracks and powder effect.
8. The line scanning experiment illustrates the utility of the spot experiment in identifying signal types within the line experiment.

While it is acknowledged that the spot experiment is not a direct representation of standard AM practice, our emphasis on fundamental mechanisms has helped us distinguish between various types of AE sources that could potentially occur during the AM process.

Our study has also allowed us to identify certain limitations of the method. For example, our study suggests that AE is a powerful technique to detect solidification cracking but is largely insensitive to pore detection. Another method, such as active source ultrasonic techniques [52], would likely be needed for direct detection of such pores. Furthermore, the low frequency "powder effect" signal will likely be a nearly continuous source of noise when printing lines (Fig. 8c) and layers in more complex structures. Yet, this noise is primarily low frequency (< 30 kHz), so, with proper filtering, high frequency AEs associated with cracks can still be distinguished even below the noise level. Other sources of noise such as previously reported bursts associated with electronic control devices [21,53] may overlap with the frequency content of the crack signals described here. In this study, we used an array of four AE sensors, so we used the relative timing of wave arrivals between the sensors (i.e. source location) to distinguish AEs from electrical noise and other sources that originated from outside the printed part. However, when only one AE sensor is used, additional time- and frequency-domain parameters may be needed to distinguish between AEs associated with cracks and other noise sources.

Finally, the quantification of crack sizes from AE analysis is possible due to an absolute calibration technique and shows that we can detect cracks down to about 40 μm in size. We encourage other researchers to utilize a ball drop or similar calibration technique since this will facilitate meaningful comparisons between studies conducted in different laboratories, regardless of the sensors or materials used. Absolute quantification of the source size (in seismic moment) will allow researchers to check the accuracy and reproducibility of their results and will facilitate the advancement of this monitoring technique.

CRediT authorship contribution statement

McLaskey Gregory C.: Writing – review & editing, Writing – original draft, Supervision, Resources, Formal analysis, Conceptualization. **Dass Adrita:** Writing – review & editing, Methodology, Investigation. **Moridi Atieh:** Writing – review & editing, Supervision, Resources, Funding acquisition. **Song Jun Young:** Writing – original draft, Visualization, Methodology, Investigation, Formal analysis, Conceptualization.

Declaration of Competing Interest

The authors declare the following financial interests/personal relationships which may be considered as potential competing interests: Adrita Dass reports financial support was provided by NASA. Atieh Moridi reports financial support was provided by National Science Foundation.

Data availability

Data from this study will be made freely available through eCommons, an online data repository maintained by Cornell University Library at https://ecommons.cornell.edu/. The data and metadata will be freely accessible via a permanent DOI number.

Acknowledgements

Atieh Moridi and Adrita Dass gratefully acknowledge funding received by the National Science Foundation CAREER Award CMMI-2046523, the NASA University Student Research Challenge Award-80NSSC21K0465, and the Office of Naval Research Young Investigator Award N00014-22-1-2420. Part of this work used the shared facilities at the Cornell Center for Materials Research, which is supported through the NSF MRSEC program (DMR-1719875). J.Y.S. and G.C.M. gratefully acknowledge a McMullen Fellowship from Cornell Engineering.

Appendix A. Supporting information

Supplementary data associated with this article can be found in the online version at doi:10.1016/j.addma.2024.104035.

References

[1] D. Gu, Y.C. Hagedorn, W. Meiners, G. Meng, R.J.S. Batista, K. Wissenbach, R. Poprawe, Densification behavior, microstructure evolution, and wear performance of selective laser melting processed commercially pure titanium, Acta Mater. 60 (2012) 3849–3860, https://doi.org/10.1016/j.actamat.2012.04.006.
[2] S. Das, M. Wohlert, J.J. Beaman, D.L. Bourell, Processing of titanium net shapes by SLS/HIP, Mater. Des. 20 (1999) 115–121, https://doi.org/10.1016/s0261-3069(99)00017-5.

[3] J. Mazumder, A. Schifferer, J. Choi, Direct materials deposition: designed macro and microstructure, Mater. Res. Soc. Symp. - Proc. 542 (1999) 51–63, https://doi.org/10.1557/proc-542-51.

[4] L.C. Zhang, D. Klemm, J. Eckert, Y.L. Hao, T.B. Sercombe, Manufacture by selective laser melting and mechanical behavior of a biomedical Ti-24Nb-4Zr-8Sn alloy, Scr. Mater. 65 (2011) 21–24, https://doi.org/10.1016/j.scriptamat.2011.03.024.

[5] F. Caiazzo, F. Cardaropoli, V. Alfieri, V. Sergi, L. Cuccaro, Experimental analysis of selective laser melting process for Ti-6Al-4V turbine blade manufacturing, in: Proceedings of the XIX Int. Symp. High-Power Laser Syst. Appl. 2012. 8677 (2013) 86771H. https://doi.org/10.1117/12.2010577.

[6] C. Yan, L. Hao, A. Hussein, P. Young, Ti-6Al-4V triply periodic minimal surface structures for bone implants fabricated via selective laser melting, J. Mech. Behav. Biomed. Mater. 51 (2015) 61–73, https://doi.org/10.1016/j.jmbbm.2015.06.024.

[7] B. Zhang, Y. Li, Q. Bai, Defect formation mechanisms in selective laser melting: a review, Chin. J. Mech. Eng. (Engl. Ed. 30 (2017) 515–527, https://doi.org/10.1007/s10033-017-0121-5.

[8] S. Alipour, A. Moridi, F. Liou, A. Emdadi, The Trajectory of additively manufactured titanium alloys with superior mechanical properties and engineered microstructures, Addit. Manuf. 60 (2022) 103245, https://doi.org/10.1016/j.addma.2022.103245.

[9] A. Dass, A. Gabourel, D. Pagan, A. Moridi, Laser based directed energy deposition system for operando synchrotron x-ray experiments, Rev. Sci. Instrum. 93 (2022), https://doi.org/10.1063/5.0081186.

[10] M. Brandt, S. Sun, M. Leary, S. Feih, J. Elambasseril, Q. Liu, High-value SLM aerospace components: from design to manufacture, Adv. Mater. Res. 633 (2013) 135–147, https://doi.org/10.4028/www.scientific.net/AMR.633.135.

[11] Q.C. Liu, J. Elambasseril, S.J. Sun, M. Leary, M. Brandt, P.K. Sharp, The effect of manufacturing defects on the fatigue behaviour of Ti-6Al-4V specimens fabricated using selective laser melting, Adv. Mater. Res. 891–892 (2014) 1519–1524, https://doi.org/10.4028/www.scientific.net/AMR.891-892.1519.

[12] H. Gong, K. Rafi, H. Gu, G.D. Janaki Ram, T. Starr, B. Stucker, Influence of defects on mechanical properties of Ti-6Al-4V components produced by selective laser melting and electron beam melting, Mater. Des. 86 (2015) 545–554, https://doi.org/10.1016/j.matdes.2015.07.147.

[13] Q.Y. Lu, C.H. Wong, Additive manufacturing process monitoring and control by non-destructive testing techniques: challenges and in-process monitoring, Virtual Phys. Prototyp. 13 (2018) 39–48, https://doi.org/10.1080/17452759.2017.1351201.

[14] K.M. Holford, M.J. Eaton, J.J. Hensman, R. Pullin, S.L. Evans, N. Dervilis, K. Worden, A new methodology for automating acoustic emission detection of metallic fatigue fractures in highly demanding aerospace environments: an overview, Prog. Aerosp. Sci. 90 (2017) 1–11, https://doi.org/10.1016/j.paerosci.2016.11.003.

[15] R. McCann, M.A. Obeidi, C. Hughes, É. McCarthy, D.S. Egan, R.K. Vijayaraghavan, A.M. Joshi, V. Acinas Garzon, D.P. Dowling, P.J. McNally, D. Brabazon, In-situ sensing, process monitoring and machine control in laser powder bed fusion: a review, Addit. Manuf. 45 (2021), https://doi.org/10.1016/j.addma.2021.102058.

[16] M. Enoki, M. Watanabe, P. Chivavibul, T. Kishi, Non-contact measurement of acoustic emission in materials by laser interferometry, Sci. Technol. Adv. Mater. 1 (2000) 157–165, https://doi.org/10.1016/S1468-6996(00)00017-6.

[17] D. Ye, G.S. Hong, Y. Zhang, K. Zhu, J.Y.H. Fuh, Defect detection in selective laser melting technology by acoustic signals with deep belief networks, Int. J. Adv. Manuf. Technol. 96 (2018) 2791–2801, https://doi.org/10.1007/s00170-018-1728-0.

[18] I. Zhirnov, D. Kouprianoff, Acoustic diagnostic of laser powder bed fusion processes, Adv. Transdiscipl. Eng. 21 (2022) 542–552, https://doi.org/10.3233/ATDE220173.

[19] N. Eschner, L. Weiser, B. Häfner, G. Lanza, Classification of specimen density in Laser Powder Bed Fusion (L-PBF) using in-process structure-borne acoustic process emissions, Addit. Manuf. 34 (2020) 101324, https://doi.org/10.1016/j.addma.2020.101324.

[20] J.R. Tempelman, A.J. Wachtor, E.B. Flynn, P.J. Depond, J.B. Forien, G.M. Guss, N. P. Calta, M.J. Matthews, Detection of keyhole pore formations in laser powder-bed fusion using acoustic process monitoring measurements, Addit. Manuf. 55 (2022) 102735, https://doi.org/10.1016/j.addma.2022.102735.

[21] M. Seleznev, T. Gustmann, J. Miriam, U. Alexander, U. Kühn, J. Kristin, H. Biermann, A. Weidner, In situ detection of cracks during laser powder bed fusion using acoustic emission monitoring, Addit. Manuf. Lett. 3 (2022) 100099, https://doi.org/10.1016/j.addlet.2022.100099.

[22] K. Wasmer, T. Le-Quang, B. Meylan, S.A. Shevchik, In situ quality monitoring in am using acoustic emission: a reinforcement learning approach, J. Mater. Eng. Perform. 28 (2019) 666–672, https://doi.org/10.1007/s11665-018-3690-2.

[23] K. Ito, M. Kusano, M. Demura, M. Watanabe, Detection and location of microdefects during selective laser melting by wireless acoustic emission measurement, Addit. Manuf. 40 (2021) 101915, https://doi.org/10.1016/j.addma.2021.101915.

[24] C.U. Grosse, M. Ohtsu, Acoustic Emission Testing: Basics for Research – Applications in Engineering, Springer-Verlag Berlin Heidelberg, 2008.

[25] N. Hsu, F. Breckenridge, Characterization and calibration of acoustic emission sensors, Mater. Eval. 39 (1981) 60–68.

[26] D. Eitzen, F. Breckenridge, Acoustic emission sensors and their calibration, Am. Soc, Nondestruct. Test. 5 (1987) 121–132.

[27] G.C. McLaskey, S.D. Glaser, Acoustic emission sensor calibration for absolute source measurements, J. Nondestruct. Eval. 31 (2012) 157–168, https://doi.org/10.1007/s10921-012-0131-2.

[28] K. Aki, P. Richards, Quantitative Seismology: Theory and Methods, 1980.

[29] A. Dass, Fundamentals of Solidification in Directed Energy Deposition Type Additive Manufacturing of Inconel 625, 2020. https://doi.org/https://doi.org/10.7298/f59s-yn90.

[30] G.C. McLaskey, S.D. Glaser, Hertzian impact: experimental study of the force pulse and resulting stress waves, J. Acoust. Soc. Am. 128 (2010) 1087, https://doi.org/10.1121/1.3466847.

[31] B.S. Wu, G.C. McLaskey, Broadband calibration of acoustic emission and ultrasonic sensors from generalized ray theory and finite element models, J. Nondestruct. Eval. 37 (1) (2018) 16, https://doi.org/10.1007/s10921-018-0462-8.

[32] T.C. Hanks, H. Kanamori, A moment magnitude scale, J. Geophys. Res. B Solid Earth 84 (1979) 2348–2350, https://doi.org/10.1029/JB084iB05p02348.

[33] G.C. McLaskey, D.A. Lockner, B.D. Kilgore, N.M. Beeler, A robust calibration technique for acoustic emission systems based on momentum transfer from a ball drop, Bull. Seismol. Soc. Am. 105 (2015) 257–271, https://doi.org/10.1785/0120140170.

[34] G. Manthei, Characterization of acoustic emission sources in a rock salt specimen under triaxial compression, Bull. Seismol. Soc. Am. 95 (2005) 1674–1700, https://doi.org/10.1785/0120040076.

[35] G.C. Mclaskey, S.D. Glaser, Temporal evolution and 3D locations of acoustic emissions produced from the drying shrinkage of concrete, Adv. Acoust. Emiss. 6 (2007) 52–57.

[36] D.C. Weckman, H.W. Kerr, J.T. Liu, The effects of process variables on pulsed Nd: YAG laser spot welds: part II. AA 1100 aluminum and comparison to AISI 409 stainless steel, Metall. Mater. Trans. B Process. Metall. Mater. Process. Sci. 28 (1997) 687–700, https://doi.org/10.1007/s11663-997-0043-1.

[37] C. Tenbrock, F.G. Fischer, K. Wissenbach, J.H. Schleifenbaum, P. Wagenblast, W. Meiners, J. Wagner, Influence of keyhole and conduction mode melting for top-hat shaped beam profiles in laser powder bed fusion, J. Mater. Process. Technol. 278 (2020) 116514, https://doi.org/10.1016/j.jmatprotec.2019.116514.

[38] W.E. King, H.D. Barth, V.M. Castillo, G.F. Gallegos, J.W. Gibbs, D.E. Hahn, C. Kamath, A.M. Rubenchik, Observation of keyhole-mode laser melting in laser powder-bed fusion additive manufacturing, J. Mater. Process. Technol. 214 (2014) 2915–2925, https://doi.org/10.1016/j.jmatprotec.2014.06.005.

[39] N. Nudelis, P. Mayr, A novel classification method for pores in laser powder bed fusion, Met. (Basel) 11 (2021) 1–16, https://doi.org/10.3390/met11121912.

[40] C.Y. Yap, C.K. Chua, Z.L. Dong, Z.H. Liu, D.Q. Zhang, L.E. Loh, S.L. Sing, Review of selective laser melting: materials and applications, Appl. Phys. Rev. 2 (2015), https://doi.org/10.1063/1.4935926.

[41] K. Kempen, B. Vrancken, S. Buls, L. Thijs, J. Van Humbeeck, J.P. Kruth, Selective laser melting of crack-free high density M2 high speed steel parts by baseplate preheating, J. Manuf. Sci. Eng. Trans. ASME 136 (2014), https://doi.org/10.1115/1.4028513.

[42] K. Kosiba, D.Y. Kononenko, D. Chernyavsky, L. Deng, J. Bednarcik, J. Han, J. van den Brink, H.J. Kim, S. Scudino, Maximizing vitrification and density of a Zr-based glass-forming alloy processed by laser powder bed fusion, J. Alloy. Compd. 940 (2023) 168946, https://doi.org/10.1016/j.jallcom.2023.168946.

[43] M. Bonamente, Statistics and Analysis of Scientific Data, Springer Nature Singapore, Singapore, 2022, https://doi.org/10.1007/978-981-19-0365-6.

[44] C.B. Scruby, G.R. Baldwin, K.A. Stacey, Characterisation of fatigue crack extension by quantitative acoustic emission, Int. J. Fract. 28 (1985) 201–222, https://doi.org/10.1007/BF00035216.

[45] A.E. Green, W. Zerna, Theoretical elasticity, Courier Corporation, 1992.

[46] H. Kanamori, D.L. Anderson, Theoretical basis of some empirical relations in seismology, Bull. Seismol. Soc. Am. 65 (1975) 1073–1095, https://doi.org/10.1785/BSSA0650051073.

[47] K.L. Telschow, R.J. Conant, Optical and thermal parameter effects on laser-generated ultrasound, J. Acoust. Soc. Am. 88 (1990) 1494–1502, https://doi.org/10.1121/1.400306.

[48] L.R.F. Rose, Point-source representation for laser-generated ultrasound, J. Acoust. Soc. Am. 75 (1984) 723–732, https://doi.org/10.1121/1.390583.

[49] C.B. Scruby, H.N.G. Wadley, R.J. Dewhurst, S.B. Palmer, D.A. Hutchins, A laser-generated standard acoustic emission source, Mater. Eval. 39 (1981) 1250–1254.

[50] A.F.H. Kaplan, J. Frostevarg, High speed imaging of powder incorporation into the melt pool in LAM, in: Proceedings of the Int. Congr. Appl. Lasers Electro-Optics, Laser Institute of America, 2016: p. 1601. https://doi.org/10.2351/1.5118551.

[51] D.R. Shelly, G.C. Beroza, S. Ide, Non-volcanic tremor and low-frequency earthquake swarms, Nature 446 (2007) 305–307, https://doi.org/10.1038/nature05666.

[52] M.V. Felice, Z. Fan, Sizing of flaws using ultrasonic bulk wave testing: a review, Ultrasonics 88 (2018) 26–42, https://doi.org/10.1016/j.ultras.2018.03.003.

[53] D.Y. Kononenko, V. Nikonova, M. Seleznev, J. van den Brink, D. Chernyavsky, An in situ crack detection approach in additive manufacturing based on acoustic emission and machine learning, Addit. Manuf. Lett. 5 (2023) 100130, https://doi.org/10.1016/j.addlet.2023.100130.